# High-Performance All-Solid-State Lithium Metal Batteries Enabled by Ionic Covalent Organic Framework Composites

Jun Huang
Lei Cheng
Zhenyang Zhang
Chen Li
Ki-Taek Bang
Albert Liem
Hang Luo
Chuan Hu
Young Moo Lee
Yingying Lu
Yanming Wang
yanming.wang@sjtu.edu.cn

Yoonseob Kim
yoonseobkim@ust.hk

Research Article

**Keywords:** Lithium metal batteries, All-solid-state electrolytes, Covalent organic frameworks, Poly(ionic liquid)

**Posted Date:** March 6th, 2024

**DOI:** https://doi.org/10.21203/rs.3.rs-4015490/v1



**Additional Declarations:**
The authors declare no competing interests.

Supplementary Figures and Supplementary Tables are not available with this version.

**Version of Record:** A version of this preprint was published at Advanced Energy Materials on April 27th, 2024. See the published version at https://doi.org/10.1002/aenm.202400762.

# High-Performance All-Solid-State Lithium Metal Batteries Enabled by Ionic Covalent Organic Framework Composites

Jun Huang[1], Lei Cheng[2], Zhenyang Zhang[2], Chen Li[1], Ki-Taek Bang[1], Albert Liem[1], Hang Luo[1], Chuan Hu[3], Young Moo Lee[3], Yingying Lu[4,5,6], Yanming Wang[2,*], and Yoonseob Kim[1,7,*]

[1]Department of Chemical and Biological Engineering, The Hong Kong University of Science and Technology, Clear Water Bay, Kowloon 999077, Hong Kong SAR, China
[2]University of Michigan - Shanghai Jiao Tong University Joint Institute, Shanghai Jiao Tong University, Shanghai 200240, P. R. China
[3]Department of Energy Engineering, College of Engineering, Hanyang University, Seoul, Korea
[4]State Key Laboratory of Chemical Engineering, Institute of Pharmaceutical Engineering, College of Chemical and Biological Engineering, Zhejiang University, Hangzhou 310027, China
[5]ZJU-Hangzhou Global Scientific and Technological Innovation Center, Zhejiang University, Hangzhou 311215, China
[6]Institute of Wenzhou, Zhejiang University, Wenzhou 325006, China
[7]Energy Institute, The Hong Kong University of Science and Technology, Hong Kong SAR, China
*To whom correspondence should be addressed: yanming.wang@sjtu.edu.cn and yoonseobkim@ust.hk

**Abstract**

Ionic covalent organic frameworks (iCOFs) are crystalline materials with stable porous structures. They hold great potential for ion transport, particularly as solid-state electrolytes (SSEs) for all-solid-state Lithium metal batteries (ASSLMBs). However, achieving an ionic conductivity of over $10^{-3}$ S $cm^{-1}$ at room temperature using pure-iCOF-based SSEs, even adding additives such as lithium salts, is challenging as the voids work as strong resistances. Thus, highly conductive iCOFs typically require quasi-solid-state configurations with organic

solvents or plasticizers. In this study, we prepared composites comprising iCOFs and poly(ionic liquid) (PIL) to make all-solid-state iCOFs electrolytes with an exceptional ionic conductivity up to $1.50 \times 10^{-3}$ S $cm^{-1}$ and a high $Li^+$ transference number of > 0.80 at room temperature. Combined experimental and computational studies showed that the co-coordination and competitive coordination mechanism established between the PIL, lithium bis(trifluoromethanesulfonyl)imide (LiTFSI) and iCOFs enabled rapid $Li^+$ transport while restricting $TFSI^-$ movement. ASSLMB cells, made of composite SSEs and $LiFePO_4$ composite cathode, demonstrated an initial discharge capacity of 141.5 mAh $g^{-1}$ at 1 C and r.t., with an impressive capacity retention of 87% up to 800 cycles. Overall, this work presents a breakthrough approach for developing advanced SSEs for next-generation high-energy-density ASSLMBs.

**Keywords**: Lithium metal batteries; All-solid-state electrolytes; Covalent organic frameworks; Poly(ionic liquid)

## Introduction

Developing next-generation lithium (Li) battery systems with a high energy density and improved safety is critical for energy storage applications, including electric vehicles, portable electronics, and power grids.[1] For this purpose, all-solid-state Li metal batteries (ASSLMBs) are promising, as they not only have high safety by replacing flammable organic solvent electrolytes with solid electrolytes, but also offer high energy density – theoretical specific capacity is 3,860 mAh $g^{-1}$.[2, 3] In this context, solid-state electrolytes (SSEs), such as polymers

and inorganic ceramics, e.g., oxides and sulfides, have been intensively investigated as critical components to meet the requirements of high-performance ASSLMBs.[4-6] Compared with conventional liquid electrolytes, inorganic ceramic SSEs can achieve high ionic conductivity and $Li^+$ transference number ($t_{Li^+}$), while exhibiting Li dendrite suppression. However, they are characterized by poor interfacial contact between SSEs and electrodes and mediocre chemical stability.[7] Polymer electrolytes show the advantages of making good interfacial contacts, ensuring Li dendrite suppression, and higher electrochemical stability. However, their further development is limited by low ionic conductivity and $t_{Li^+}$ at room temperature (r.t.).[8]

Porous crystalline polymers (PCPs), a new generation of polymeric electrolytes, such as covalent organic frameworks (COFs), show great potential as solid electrolyte materials owing to their high stability, rapid and selective $Li^+$ transport, and facile synthesis and scale-up.[9-11] Compared with inorganic ceramics, PCP-based SSEs have improved interfacial contact, ensured Li dendrite suppression, higher ionic conductivity and $t_{Li^+}$, and improved electrochemical stability.[12] Since the first report on the COF synthesis through reversible condensation reactions in 2005,[13] studies have been conducted on COFs to develop their synthetic scopes, and the ones with ionic linkages were reported in 2015.[14] Ionic COFs (iCOFs) have received significant attention for battery applications due to their outstanding electrochemical properties, enabling them stability and ensuring dendrite suppression,[15, 16] and defined nanoscale channels,[17, 18] endowing them with excellent conduction properties.[19-21] However, the first generation of iCOF-based SSEs containing pure-iCOFs exhibited high contact resistance, due to the presence of a large volume of voids between the COF powders, resulting in lower ionic conductivity (**Fig. 1a**). For example, sulfonated COF SSEs showed a

conductivity of 2.70 × $10^{-5}$ S $cm^{-1}$ at r.t.[22] Another type of solution-processable COF SSE demonstrated a conductivity of 3.21 × $10^{-5}$ S $cm^{-1}$ at 20 °C.[23] Some other studies have shown that the conductivity of pure-iCOF-based SSEs can be increased by filling the voids with ion-conductive materials, such as polymers or metal oxides. For example, a composite SSE consisting of vinylene-linked iCOFs incorporating polyethylene oxide showed an improved ionic conductivity of 4.17 × $10^{-4}$ S $cm^{-1}$ at 20 °C.[24] However, the ionic conductivity was still unsatisfactory for practical application, and the transference number remained low. Researchers have addressed this low conductivity issue by adding a notable amount, around 20 wt.%, of organic solvents or plasticizers, such as propylene carbonate (**Fig. 1b**). This type of quasi-solid-state electrolyte have achieved high conductivity in the range of $10^{-4}$ to $10^{-3}$ S $cm^{-1}$ at r.t..[25, 26] Using this method, imidazolate COFs obtained the high ionic conductivity of 7.20 × $10^{-3}$ S $cm^{-1}$ at 25 °C.[26] Our group has also made a notable advancement in terms of high conductivity, 9.80 × $10^{-3}$ S $cm^{-1}$at r.t., and $t_{Li^+}$, 0.92, from anthraquinone-based silicate COFs.[21] This way of making quasi-solid-state electrolyte is a practical way for engineering applications. However, adding organic solvents keeps the safety concerns, and *ideal solid electrolytes for ASSLMBs should be solvent-free for ultimate safety and long-term use*.

Here, we report a breakthrough by making a solid-state composite of iCOFs with ion-conductive polymers. This approach enabled increased ionic conductivity and improved interfacial contact, chemical stability, and electrochemical stability significantly in a balanced manner compared with pure iCOFs. We used poly(ionic liquid) (PIL) as an ion-conductive polymeric matrix and iCOFs as fillers for the composite system. PIL refers to a class of ionic liquid polymers with ionic groups incorporated into the polymer backbone.[27] The PIL is

expected to enhance $Li^+$ conduction by anchoring the bis(trifluoromethanesulfonyl)imide anions ($TFSI^-$) to the cationic sites on the PIL, enabling the free movement of $Li^+$. This co-coordination mechanism is known to enable rapid and selective transport of counter ions.[28, 29] Moreover, when $Li^+$ and $TFSI^-$ enter the iCOFs' pores, a coordination interplay occurs between $Li^+$, the anionic part of iCOFs, and $TFSI^-$, to reject the entrance of $TFSI^-$, thus selectively transporting $Li^+$ (**Fig. 1c**). We demonstrate this co-coordination mechanism for the first time in the all-solid-state using a model system of TpPa-$SO_3$Li as iCOF fillers (**Fig. 1d**, a type of $Li^+$ coordinating sulfonate COFs; Tp and Pa mean 1,3,5-triformylphloroglucinol and 1,4-phenylenediamine, respectively[22]) and p(BVIm-TFSI) as the PIL matrix (**Fig. 1f**; poly(1-butyl-3-vinylimidazolium) with bis(trifluoromethanesulfonyl)imide)). We chose imidazolium-based polyethylene as PIL in this study as it is easy to be synthesized, has a wide synthetic scope, and have outstanding chemical and electrochemical stability.[30, 31] To show the generality of this composites' co-coordination mechanisms, we also present another composite system based on DMTHA-Si-Li (**Fig. 1e**, a type of $Li^+$ coordinating silicate COFs; DMTHA means 9,10-dimethyl-2,3,6,7-tetrahydroxyanthracene).

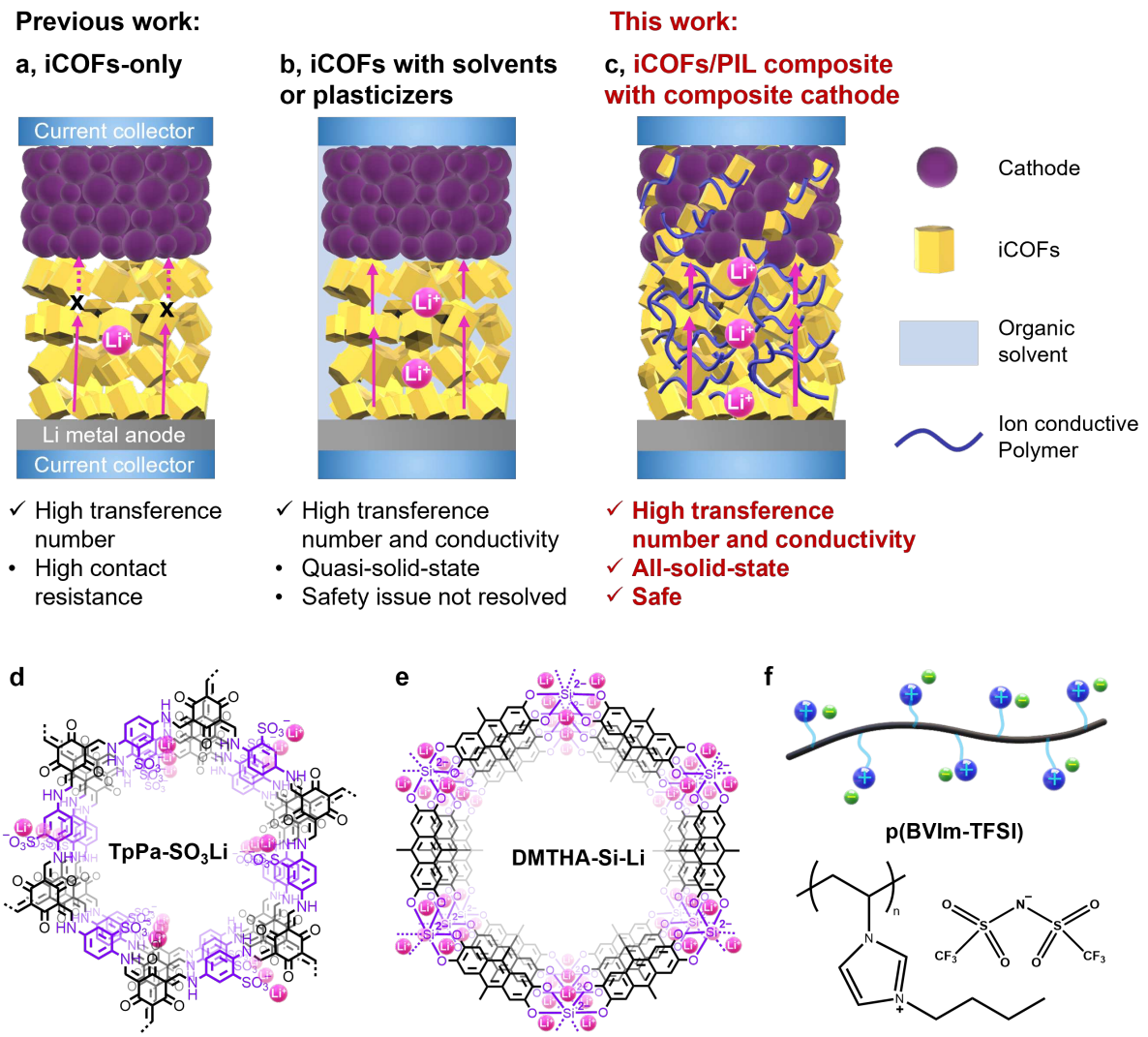


**Figure 1. Overall scheme of the ionic covalent organic frameworks (iCOFs) and poly(ionic liquids) (PIL) design. a-c, Schematic of $Li^+$ transport in previous generations of iCOF-based electrolytes and our design. a,** iCOFs-only structure showing a large volume of voids, making high contact resistance. **b,** iCOFs with solvent or plasticizers showing improved conduction while remaining as quasi-solid-state electrolytes. **c,** iCOFs/PIL composite showing rapid $Li^+$ conduction and high selectivity, working as safe all-solid-state electrolytes. **d-f,** Chemical structures of TpPa-$SO_3$Li iCOFs, DMTHA-Si-Li iCOFs, and p(BVIm-TFSI) PIL, respectively.

With optimized composite conditions (See **Fig. 3** and **Supporting Information (SI)** for detailed conditions and related properties.), we obtained a high ionic conductivity of > 1.30 × $10^{-3}$ S $cm^{-1}$ at r.t. and near single-ion conductive $t_{Li^+}$ > 0.8, which are the highest among solvent- and plasticizer-free COF-based SSEs. The mechanisms underlying such high

electrochemical properties were unveiled by $^{7}Li$ solid-state magic-angle-spinning (MAS) nuclear magnetic resonance (NMR) characterization and molecular dynamics (MD) simulations. Then, we fabricated ASSLMB coin cells with the iCOFs/PIL composite SSEs paired with composite $LiFePO_4$ cathodes. The cells with TpPa-$SO_3Li$/p(BVIm-TFSI) and DMTHA-Si-Li/p(BVIm-TFSI) SSEs showed initial discharge capacities of 138.5 and 141.5 mAh $g^{-1}$ at 1 C and r.t., and 81 and 87% of them were retained after 800 cycles, respectively. In the following sections, we thoroughly present comprehensive characterizations, mechanism investigation, and device performances.

**Results and discussion**

First, TpPa-$SO_3Li$, a type of sulfonate COFs, was synthesized through a Schiff-base condensation reaction using 1,3,5-triformylphloroglucinol and 1,4-phenylenediamine-2-sulfonic acid, followed by cation exchange from $H^+$ to $Li^+$ (**Fig. 1d**; See **Section 2. Synthesis and fabrication in the SI** for detailed synthetic procedures). The formation of the characteristic keto-enamine linkage in TpPa-$SO_3Li$ was confirmed by the characteristic Fourier transform infrared (FT-IR) spectrum.[22, 32] The spectrum exhibited prominent peaks at 1568 $cm^{-1}$ corresponding to the C=C stretch and at 1223 $cm^{-1}$ corresponding to the C–N stretch, confirming the presence of the keto-enamine linkage (**Fig. S6**). X-ray photoelectron spectroscopy (XPS) results showed the formation of Li–O coordination, indicating $Li^+$ existed near the COFs (**Fig. S7**). DMTHA-Si-Li, a type of silicate COFs, was synthesized via a condensation reaction involving DMTHA monomer and silicon dioxide at 180 ℃ for 4 days. (**Fig. 1e**; See **Section 2. Synthesis and fabrication in the SI** for detailed synthetic procedures).

XPS analysis of DMTHA-Si-Li iCOFs showed the formation of connecting networks through Si–O bonds, and the detection of Li–O bonds indicated the incorporation of $Li^+$ into the COF (**Fig. S8**). Furthermore, powder X-ray diffraction (PXRD) and scanning electron microscopy (SEM) results demonstrated the high crystallinity and uniform nanoplatelet morphology of DMTHA-Si-Li iCOFs (**Fig. S9**), consistent with the findings from previous studies.[21, 33] The as-synthesized TpPa-$SO_3$Li iCOFs exhibited strong characteristic peaks at 4.6 and 26.7°, corresponding to a 2D layered structure and π–π stacking interactions among the layers, respectively (**Fig. 2a**). Similarly, the synthesized DMTHA-Si-Li iCOFs displayed a high level of crystallinity, as indicated by characteristic peaks consistent with previously reported results,[33] thereby validating the layered crystalline structure of the 2D COFs. For the composite sample, containing 15.6 wt.% of TpPa-$SO_3$Li and 12.8 wt.% of DMTHA-Si-Li, the characteristic peaks were decreased owing to the scattering of incident light by the polymer matrix. The SEM images of TpPa-$SO_3$Li and DMTHA-Si-Li iCOFs also displayed their crystalline and uniform morphology (**Figs. S9** and **S10**). TpPa-$SO_3$Li and DMTHA-Si-Li iCOFs exhibited a Brunauer–Emmett–Teller surface area of 320 $m^2\ g^{-1}$ and 956 $m^2\ g^{-1}$, respectively (**Fig. 2b**).

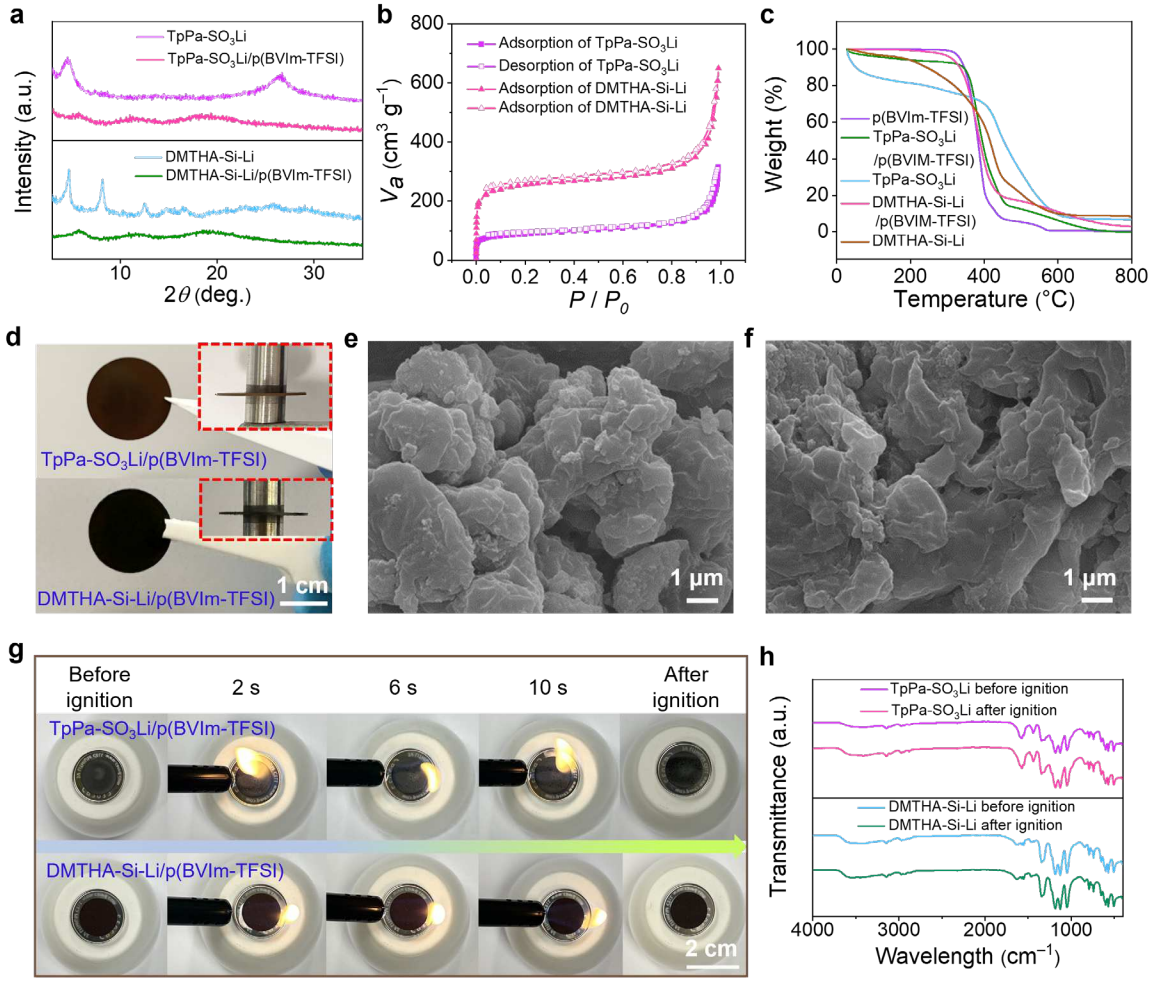


**Figure 2. Characterization of the iCOF/PIL composites. a,** Powder X-ray diffraction (PXRD) patterns of TpPa-$SO_3$Li, TpPa-$SO_3$Li/p(BVIm-TFSI) composite, DMTHA-Si-Li, and DMTHA-Si-Li/p(BVIm-TFSI) composite. **b,** Nitrogen gas sorption isotherms measured at 77 K for TpPa-$SO_3$Li and DMTHA-Si-Li iCOFs. **c,** Thermogravimetric analysis curves of p(BVIm-TFSI), TpPa-$SO_3$Li, DMTHA-Si-Li, the TpPa-$SO_3$Li/p(BVIm-TFSI) composite, and the DMTHA-Si-Li/p(BVIm-TFSI) composite. **d,** Photographic images of the composites. Insets are digital images with cross-sectional views. **e–f,** Scanning electron microscopy (SEM) images of the TpPa-$SO_3$Li/p(BVIm-TFSI) composite, and the DMTHA-Si-Li/p(BVIm-TFSI) composite, respectively. **g,** Photographic images of ignition test on the TpPa-$SO_3$Li/p(BVIm-TFSI) and DMTHA-Si-Li/p(BVIm-TFSI) composites. **h,** Fourier-transform infrared (FT-IR) spectra of the TpPa-$SO_3$Li/p(BVIm-TFSI) and DMTHA-Si-Li/p(BVIm-TFSI) composites before and after the ignition test.

The p(BVIm-TFSI) PIL was synthesized through a radical polymerization method using 1-butyl-3-vinylimidazolium, followed by ion exchange (See **Section 2. Synthesis and fabrication in the SI** for detailed synthetic procedures). XPS results confirmed the successful

ion exchange, with $TFSI^-$ identified as the counterion (**Fig. S11**). The resulting p(BVIm-TFSI) featured a sufficiently high molecular weight to function as a composite matrix. We measured the viscosity of p(BVIm-TFSI) as it was not soluble in common solvents used for gel permeation chromatography, and it was obtained as 7.54 dL $g^{-1}$ (**Fig. S12**). For comparison, p(BVIm-Br) (with $Br^-$ as the counterion of the PIL) exhibited a slightly lower viscosity of 7.31 dL $g^{-1}$ (**Fig. S13**). A high viscosity, typically exceeding 4 dL $g^{-1}$, plays a significant role in enhancing the formation of free-standing membranes and improving their stability.[34] Thermal stability is essential for SSEs in high-safety ASSLMBs, as it ensures that the SSEs maintain their original chemical structure and compositions during long-term charge–discharge processes. Although imine-linked COFs are characterized by excellent chemical stability, their thermal stability is not as high as expected. Thermogravimetric analysis showed that the TpPa-$SO_3$Li iCOF lost 14.9 and 23.0% of its weight when heated up to 100 and 300 °C, respectively. DMTHA-Si-Li iCOF exhibited a weight loss of 2.9 and 17.0% upon heating up to 100 and 300 °C, respectively (**Fig. 2c**). However, the p(BVIm-TFSI) PIL, an imidazolium-functionalized polyethylene, showed excellent thermal stability owing to carbon–carbon single bond backbone and stable imidazolium groups. It exhibited only a 0.7% weight loss when heated up to 300 °C. Thus, the TpPa-$SO_3$Li/p(BVIm-TFSI) and DMTHA-Si-Li/p(BVIm-TFSI) composites demonstrated significantly improved thermal stability compared to pure iCOFs. The TpPa-$SO_3$Li/p(BVIm-TFSI) and DMTHA-Si-Li/p(BVIm-TFSI) composite showed 7.3 and 3.6% weight decrease when heated up to 300 °C, respectively, which are above-satisfactory for thermally stable solid electrolytes. These decreases were minimal and even less than that observed in one of the most thermally stable benzoxazole COFs.[35]

The synthesized iCOFs and PIL were used to create composite pellets with a uniform dispersion of the iCOF powders (**Fig. 2d–f**). SEM images of the samples, TpPa-$SO_3$Li/p(BVIm-TFSI) and DMTHA-Si-Li/p(BVIm-TFSI), show the composite morphology, containing polymer matrix and fillers (**Figs. 2e, f,** and **S14**). For composite preparations, p(BVIm-TFSI) was first dissolved in acetonitrile, and then TpPa-$SO_3$Li or DMTHA-Si-Li iCOFs were added to the mixture under stirring conditions to ensure the uniformity of the composite (See **SI** for detailed procedures). The high uniformity of the composite was confirmed by performing energy dispersive X-ray (EDX) mapping (**Figs. S15** and **S16**). As one of the first steps of important tests in SSEs, we conducted ignition tests to demonstrate the thermal stability of both TpPa-$SO_3$Li/p(BVIm-TFSI) and DMTHA-Si-Li/p(BVIm-TFSI) composites. The composites exhibited non-flammability when exposed to a torch flame for 10 s and remained intact after the test (**Fig. 2g**). Additionally, we analyzed the chemical structure and properties of the torched composite SSEs. Our findings revealed that the FT-IR spectra of the SSEs before and after the ignition test were nearly identical, indicating the stability of the SSEs and the preservation of their chemical bonds (**Fig. 2h**). Moreover, the composite's properties examined before and after the ignition tests, such as ionic conductivity, will be expounded upon in subsequent analyses and discussions.

For the optimized iCOFs/PIL composites, 15.6 wt.% of TpPa-$SO_3$Li showed an ionic conductivity of $1.32 \times 10^{-3}$ S cm$^{-1}$ at r.t. and $t_{Li^+}$ of 0.82, and 12.8 wt.% of DMTHA-Si-Li showed an ionic conductivity of $1.50 \times 10^{-3}$ S cm$^{-1}$ at r.t. and $t_{Li^+}$ of 0.80 (Note that we used composites with these fractions for most experiments unless otherwise stated. See **Fig. 3a** and **3b** for systematic studies of conductivity depending on the iCOF weight fraction.) Expectedly,

as the iCOF contents increased, the conductivity decreased significantly. For instance, pure TpPa-$SO_3Li$ COFs exhibited a conductivity of $2.70 \times 10^{-5}$ S $cm^{-1}$ at r.t. with a $t_{Li^+}$ of 0.90; and DMTHA-Si iCOFs, even with the inclusion of 60 wt.% solvent (ethylene carbonate/diethyl carbonate, v/v = 1:1), exhibited a low ionic conductivity of $1.30 \times 10^{-4}$ S $cm^{-1}$ at r.t.[25] Of course, a pure PIL sample without LiTFSI was almost non-conductive (**Fig. S17**). These conductivity behaviors showed that pure iCOF SSEs have lower conductivity as the interfaces of crystalline COF powders work as strong resistance, while p(BVIm-TFSI) ion conductive polymer works for sealing the voids and helping $Li^+$ transport. Thus, our composite showing two orders of magnitude higher conductivity than pure samples is a breakthrough that can be widely used in all-solid-state devices. Furthermore, after the ignition test, TpPa-$SO_3Li$/p(BVIm-TFSI) and DMTHA-Si-Li/p(BVIm-TFSI) composite SSEs maintained high ionic conductivities of $1.10 \times 10^{-3}$ and $1.29 \times 10^{-3}$ S $cm^{-1}$ at r.t., which are 84.0 and 87.2% of the original samples, respectively (**Figs. 3c, S18,** and **S19**).

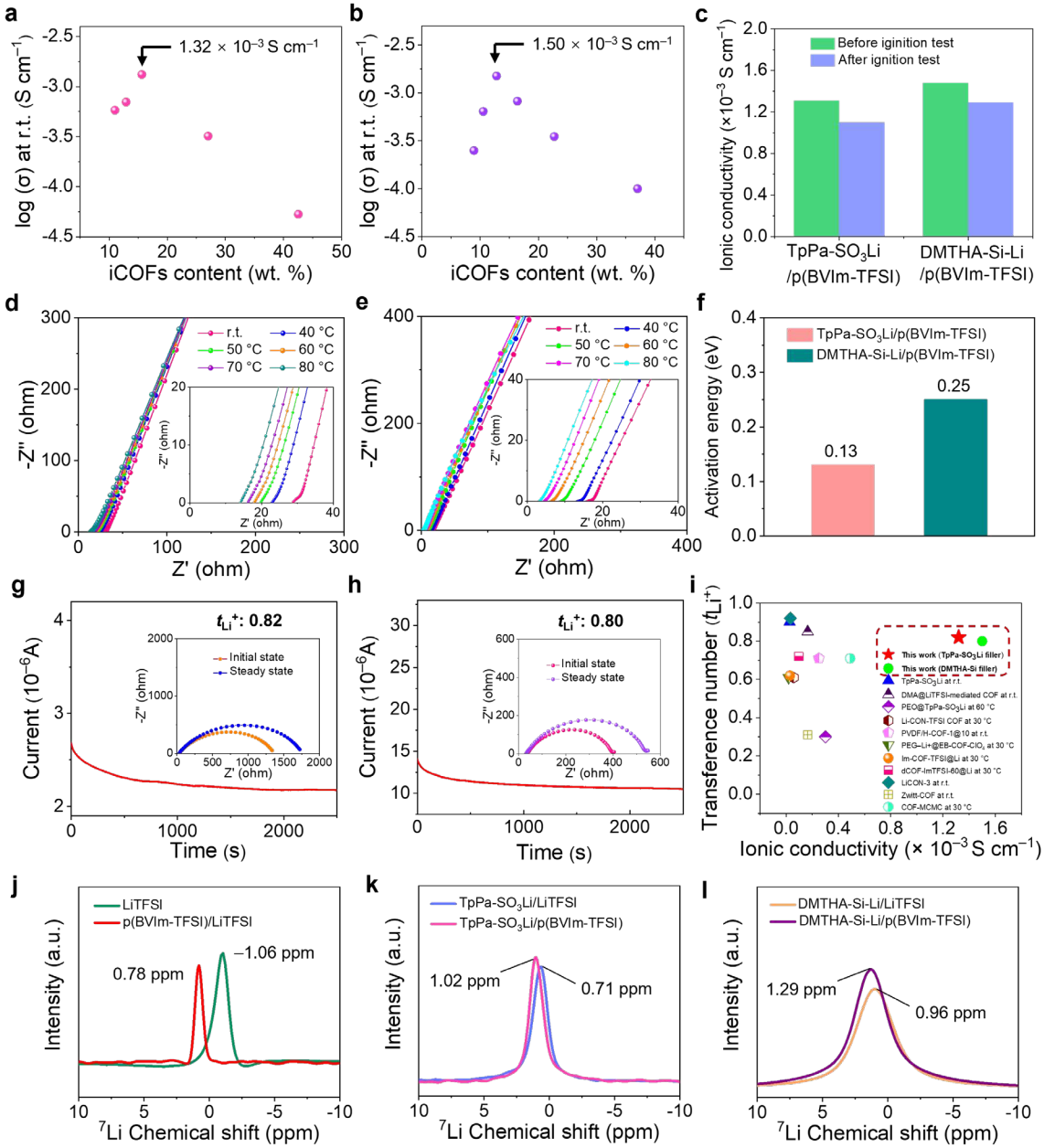


**Figure 3. Ionic conductivity and transference number of the iCOF/PIL SSEs, and the mechanism of fast $Li^+$ transport**. **a, b,** Ionic conductivities of TpPa-$SO_3$Li/p(BVIm-TFSI) and DMTHA-Si-Li/p(BVIm-TFSI) composite SSEs with various iCOF contents, respectively. **c**, Comparison of ionic conductivities of TpPa-$SO_3$Li/p(BVIm-TFSI) and DMTHA-Si-Li/p(BVIm-TFSI) SSEs before and after the ignition test. **d, e,** Nyquist plots of electrochemical impedance spectroscopy (EIS) measurements at various temperatures for TpPa-$SO_3$Li/p(BVIm-TFSI) and DMTHA-Si-Li/p(BVIm-TFSI), respectively. Insets are zoomed-in Nyquist plots. **f**, Activation energies of TpPa-$SO_3$Li/p(BVIm-TFSI) and DMTHA-Si-Li/p(BVIm-TFSI) SSEs. **g, h,** Chronoamperometry profiles of Li|TpPa-$SO_3$Li/p(BVIm-TFSI)|Li and Li|DMTHA-Si-Li/p(BVIm-TFSI)|Li symmetric cells, respectively. Insets are Nyquist plots of EIS measurements before and after polarization. **i,** Comparison of ionic conductivities and $t_{Li^+}$ for different all-solid-state, without any plasticizers, iCOFs-based SSEs. References: TpPa-$SO_3$Li at r.t.,[22] DMA@LiTFSI-mediated COF at r.t.,[36] Polyethylene

oxide@TpPa-$SO_3Li$ at 60 °C,[37] Li-CON-TFSI COF at 30 °C,[38] PVDF/H-COF-1@10 at r.t.,[39] PEG–$Li^+$@EB-COF-$ClO_4$ at 30 °C,[40] Im-COF-TFSI@Li at 30 °C,[41] dCOF-ImTFSI-60@Li at 30 °C,[42] LiCON-3 at r.t.,[23] Zwitt-COF at r.t.,[43] COF-MCMC at 30 °C.[44] **j–l,** $^7$Li solid-state magic-angle-spinning (MAS) nuclear magnetic resonance (NMR) spectrum comparison of LiTFSI and p(BVIm-TFSI)/LiTFSI (j), TpPa-$SO_3Li$/p(BVIm-TFSI) and TpPa-$SO_3Li$/LiTFSI (k), and DMTHA-Si-Li/p(BVIm-TFSI) and DMTHA-Si-Li/p(BVIm-TFSI)/LiTFSI (l).

To understand such high conductivity values from solvent- and plasticizer-free all-solid-state iCOF-based electrolytes, we looked at the synergy between PIL and iCOFs. We initially measured the conductivity of p(BVIm-TFSI)/LiTFSI without the presence of iCOFs, and found that these cases exhibited very low ionic conductivities, with the highest value being $2.30 \times 10^{-6}$ S $cm^{-1}$ at r.t. (**Fig. S20** and **Table S1**). Afterward, we obtained Nyquist plots of TpPa-$SO_3Li$/p(BVIm-TFSI) and DMTHA-Si-Li/p(BVIm-TFSI) at various temperatures (**Figs. 3d, 3e, S21,** and **S22**) to learn that activation energies are 0.13 and 0.25 eV, respectively (**Figs. 3f, S23** and **S24**). In contrast, pure-TpPa-$SO_3Li$ SSE showed an activation energy of 0.18 eV.[22] The DMTHA-Si-Li SSE, incorporating 60 wt.% solvent (ethylene carbonate/diethyl carbonate, v/v = 1:1), exhibited an activation energy of 0.15 eV.[25] Previous studies showed that pure iCOFs have single-ion conductive $t_{Li^+}$, often > 0.9. Our TpPa-$SO_3Li$/p(BVIm-TFSI) and DMTHA-Si-Li/p(BVIm-TFSI) composites SSEs showed comparable $t_{Li^+}$ of 0.82 and 0.80, respectively (**Fig. 3g, 3h**). Overall, the composites succeeded in boosting the conductivities while minimally sacrificing the $t_{Li^+}$. Of course, p(BVIm-TFSI)/LiTFSI exhibited a very low $t_{Li^+}$ value of 0.02 (**Fig. S25**). The comparison of the ionic conductivities and $t_{Li^+}$ values of iCOF-based SSEs, which are solvent- and plasticizer-free all-solid-state electrolytes, demonstrated that our sample exhibited the best performance (**Fig. 3i**). All the previous literature reported ionic conductivities below $10^{-3}$ S $cm^{-1}$. Furthermore, we prepared TpPa-

$SO_3Li$/LiTFSI and DMTHA-Si-Li/LiTFSI SSEs without p(BVIm-TFSI) as control groups. The TpPa-$SO_3Li$/LiTFSI and DMTHA-Si-Li/LiTFSI SSEs showed ionic conductivities of 4.20 × $10^{-4}$ and 4.80 × $10^{-4}$ S $cm^{-1}$ and $t_{Li^+}$ values of 0.63 and 0.60, respectively (**Figs. S26** and **S27**). All these analyses and control experiments indicate that the synergy between iCOF and PIL components, not by any single components, in achieving high ionic conductivity and a $t_{Li^+}$ value is critical.

Thus, we looked at $Li^+$-$TFSI^-$-$PIL^+$ co-coordination assemblies in the iCOF/PIL SSEs as a key factor in achieving such exceptional performance. For this, we analyzed $^7$Li solid-state MAS NMR spectrum of samples and conducted MD simulations. First, we noted that a $Li^+$-$TFSI^-$-$PIL^+$ co-coordination arrangement would be formed when LiTFSI salts were added to p(BVIm-TFSI). As the PIL is cationic and $TFSI^-$ is already coordinated to $PIL^+$, it is logical to picture that $Li^+$ is coordinated to $TFSI^-$ to form a co-coordination arrangement. This co-coordination structure immobilized $TFSI^-$ to the PIL backbone while allowing $Li^+$ to move freely around the SSE.[28, 29] As the Li salt content increased within a certain range, the conductivity also increased, attributable to the "polymer in salt" mechanism.[45, 46] This mechanism differs significantly from that associated with conventional polymer electrolytes, highlighting the unique role of cationic polymer electrolytes. We observed those less-bound $Li^+$ from $^7$Li solid-state MAS NMR. Pure LiTFSI showed a highly shielded environment for Li, while p(BVIm-TFSI)/LiTFSI showed a significant downshift of 1.84 ppm to be 0.78 ppm. Additionally, a smaller full width at half maximum (FWHM) value from p(BVIm-TFSI)/LiTFSI, 104.8 Hz, was obtained (**Fig. 3j**; Note that the pure LiTFSI has FWHM of 192.3 Hz). This downfield shift and smaller FWHM indicate a reduction in the electron cloud

surrounding the $Li^+$ nucleus, promoting the dissociation of $Li^+$ from the coordination sites and enhanced mobility of $Li^+$.[44, 47] Notably, the iCOFs/PIL composites showed a downfield shift compared to the iCOFs/LiTFSI complex, indicating that composite SSEs can enable a faster $Li^+$ conduction than the iCOFs/LiTFSI complex. For example, the TpPa-$SO_3$Li/p(BVIm-TFSI) and DMTHA-Si-Li/p(BVIm-TFSI) composite SSEs showed a downfield shift of 0.31 and 0.33 ppm over their counterparts of TpPa-$SO_3$Li/LiTFSI and DMTHA-Si-Li/LiTFSI SSEs, respectively (**Fig. 3k** and **3l**). In addition, the composite SSEs exhibited a smaller FWHM value, e.g., 219.6 and 629.0 Hz for TpPa-$SO_3$Li/p(BVIm-TFSI) and DMTHA-Si-Li/p(BVIm-TFSI), while the iCOFs/LiTFSI complex showed 238.6 and 644.6 Hz, respectively.

With experimental evidence of the co-coordination mechanism, we performed MD simulations for the TpPa-$SO_3$Li/p(BVIm-TFSI) system (**Fig. 4**). First, an interface model between TpPa-$SO_3$Li iCOFs and p(BVIm-TFSI) PIL was constructed by placing a conformationally relaxed PIL block on top of a stack of iCOFs (**Fig. 4a**). Following a 20 ns NPT (constant-temperature, constant-pressure ensemble) simulation at 473 K and 1 bar, $TFSI^-$ were found to have a greater propensity to penetrate the pores of iCOFs compared with PIL. To illustrate this trend more clearly, we provided the spatial distribution along the *z*-direction of the iCOF region for each species (PIL, $TFSI^-$, and $Li^+$), where *N* represents the number of molecules in each scanned region (with a bin size of 4 Å), and *H* is the height. While the PIL chains did not pass through the iCOF pores, a significantly larger number of $TFSI^-$ were distributed uniformly across the pores, suggesting $TFSI^-$ and $Li^+$ were the dominant species filling the iCOFs' pores in the composite electrolyte system, which should be related to the conductivity enhancement. To further investigate this effect, a series of MD simulations were

conducted, in which $TFSI^-$ and $Li^+$ were inserted into iCOFs at different number ratios ($R$) of LiTFSI to iCOFs (**Fig. 4b**). For the pure iCOFs, $R$ was zero. As $R$ increased, the self-diffusion coefficient of $Li^+$ ($D_{Li+}$) increased almost linearly, while the self-diffusion coefficient of $TFSI^-$ ($D_{TFSI-}$) remained low. Specifically, when $R$ reached 0.424, $D_{Li+}$ was almost 10 times $D_{TFSI-}$ (**Table S2**). The pronounced increase in $Li^+$ diffusivity was a major contributor to the overall conductivity improvement of the composite electrolyte. Furthermore, the large disparity between $D_{TFSI-}$ and $D_{Li+}$ may be a probable reason for the high transference number of the electrolyte. The $Li^+$ conductivity could potentially be even higher at larger $R$ values. However, the iCOF volume increased when more LiTFSI molecules were inserted, i.e., when $R > 0.424$. These higher-$R$ cases were not explored in this study. To provide mechanistic insights into the calculated self-diffusion coefficients, we calculated the radial distribution functions (RDFs) of $Li^+$ in relation to negatively charged atoms in $SO_3^-$ and $TFSI^-$ (**Fig. 4c**). When LiTFSI molecules were added to the system, the RDFs featured peaks of $Li^+$ close to peaks associated with $TFSI^-$ and $SO_3^-$. Compared with the RDF of pure iCOFs, the pores of which were filled by more $TFSI^-$ and $Li^+$ than those of the composite system, the RDFs of the composite system featured lower and wider peaks, indicating $SO_3^-$/$TFSI^-$ co-coordination. This competitive relationship between $SO_3^-$ and $TFSI^-$ facilitated $Li^+$ dissociation and potentially introduced more metastable states along the hopping path of $Li^+$, creating a fast track for $Li^+$ diffusion. This computational study agree with the results obtained from $^7Li$ solid-state MAS NMR spectroscopy (**Fig. 3k**).

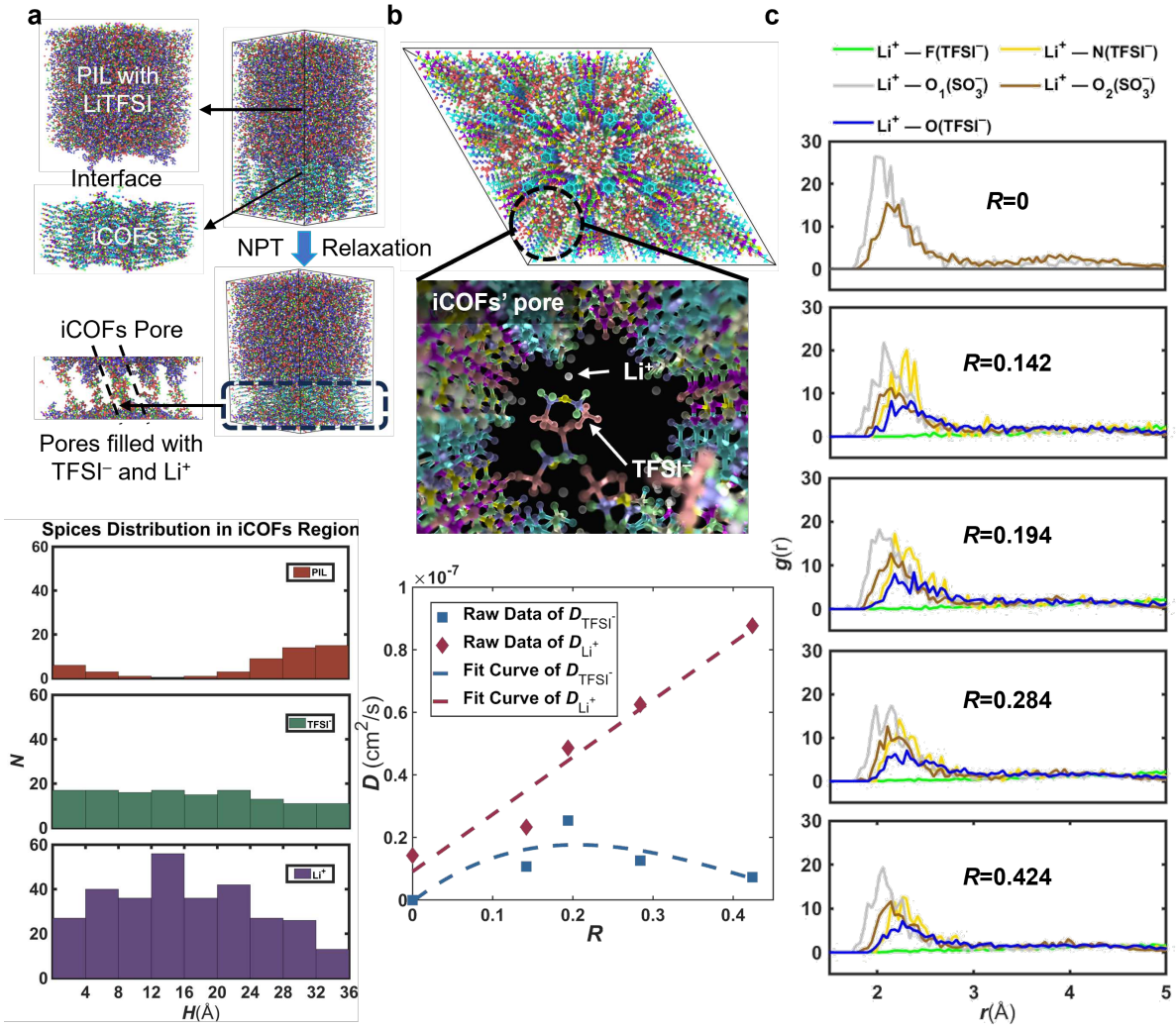


**Figure 4. Molecular dynamics simulations of the TpPa-SO$_3$Li/p(BVIm-TFSI) composite SSE system**. **a**, Molecular distribution of p(BVIm-TFSI) PIL, TFSI$^-$, and Li$^+$ in the TpPa-SO$_3$Li iCOF. **b**, Variation trend of diffusivities of TFSI$^-$ and Li$^+$ in the iCOFs/LiTFSI system with different LiTFSI-to-iCOF ratios (*R*). **c**, Radial distribution functions of Li$^+$ in relation to negatively charged atoms in SO$_3^-$ and TFSI$^-$ at a series of *R* values.

With our mechanistic understanding, we moved on to using the composites as SSEs and fabricating cells to measure electrochemical properties. The TpPa-SO$_3$Li/p(BVIm-TFSI) composite SSE showed an oxidation potential exceeding 4.5 V vs. Li/Li$^+$ at a scan rate of 1 mV s$^{-1}$ (**Fig. 5a**). Likewise, the DMTHA-Si-Li/p(BVIm-TFSI) exhibited a higher oxidation potential of approximately 4.8 V. In comparison, TpPa-SO$_3$Li and DMTHA-Si-Li individually displayed relatively lower oxidation potentials of approximately 4.0 V and 4.7 V, respectively.

Notably, p(BVIm-TFSI)/LiTFSI had a high oxidation potential of approximately 5.0 V, indicating stable nature of carbon–carbon single bond backbone. This discrepancy suggests that the incorporation of p(BVIm-TFSI) contributes to the high electrochemical stability to the composite SSEs. Such high oxidizing potential showed the promise of our composite SSEs under high voltage working conditions. To investigate the compatibility of the composite SSEs with Li metal electrodes and their ability to suppress Li dendrite formation, Li symmetric coin cells, denoted as Li|TpPa-$SO_3$Li/p(BVIm-TFSI)|Li and Li|DMTHA-Si-Li/p(BVIm-TFSI)|Li, were fabricated and tested via galvanostatic charging and discharging at a current density of 0.3 mA $cm^{-2}$ for 2 h per cycle. Li|TpPa-$SO_3$Li/p(BVIm-TFSI)|Li exhibited stable Li plating/stripping profiles at r.t., with no significant increase or fluctuation in overpotential for up to 1,200 h (**Fig. 5b**). In contrast, the Li|p(BVIm-TFSI)/LiTFSI|Li and Li|TpPa-$SO_3$Li|Li cells exhibited significant overpotentials up to 5 and 4.2 V over the time of 45 and 176 h, respectively. This failure should be due to inefficient transport of $Li^+$ through the single component, either iCOFs or PIL, SSEs. Similarly, the Li|DMTHA-Si-Li/p(BVIm-TFSI)|Li cells displayed stable Li plating/stripping profiles at r.t., with no noticeable increase or fluctuation in overpotential for up to 1200 h (**Fig. 5d**). In comparison, the Li|DMTHA-Si-Li|Li cell demonstrated a considerable overpotential of 3.1 V for 250 h.

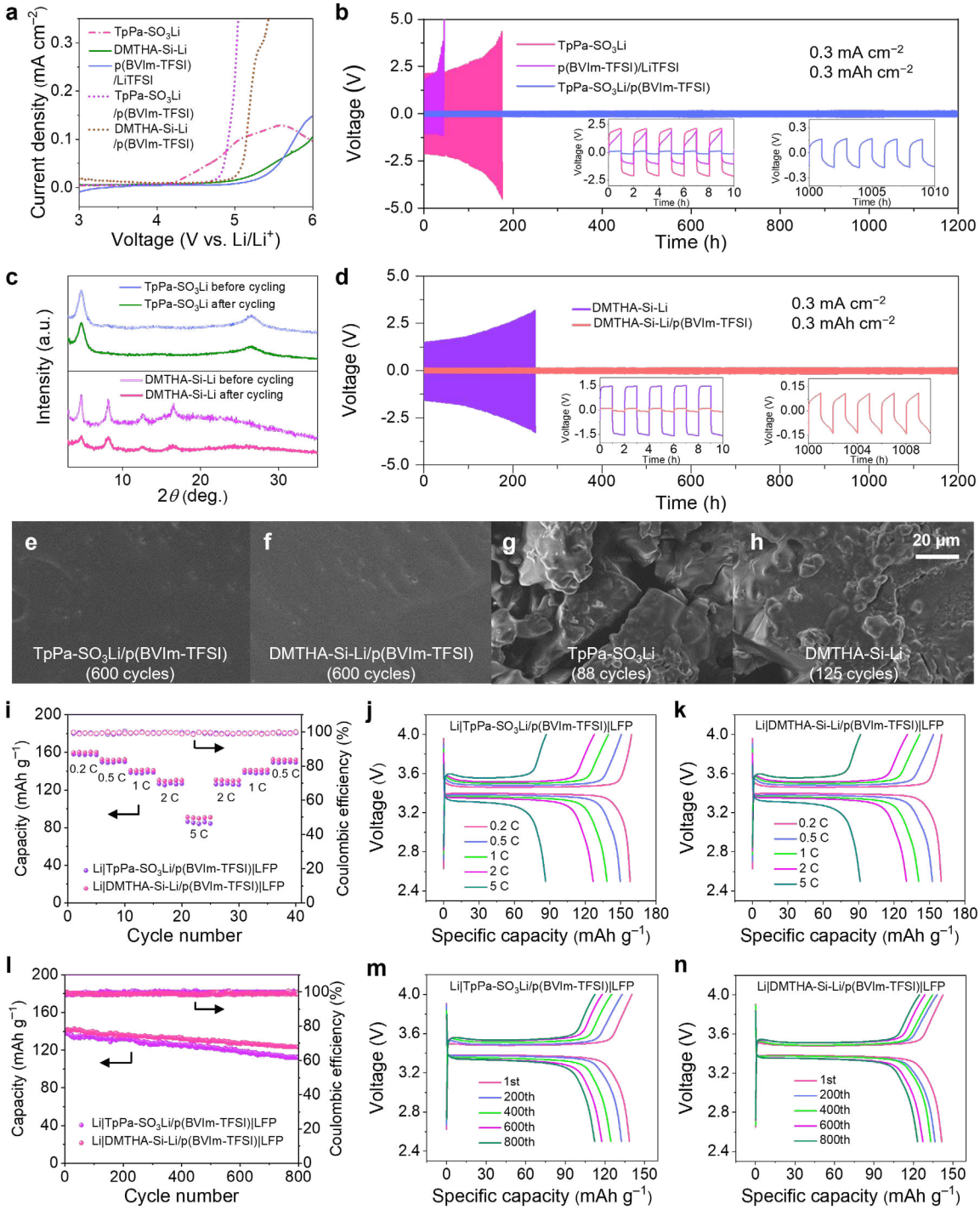


**Figure 5. Electrochemical stability window of the composite SSEs, and the electrochemical performance of Li|SSE|Li symmetric coin cells and Li|SSE|LiFePO$_4$ coin cells.** All the measurements were conducted at r.t. **a,** Electrochemical stability window of the TpPa-SO$_3$Li, DMTHA-Si-Li, p(BVIm-TFSI)/LiTFSI, TpPa-SO$_3$Li/p(BVIm-TFSI), and DMTHA-Si-Li/p(BVIm-TFSI) SSEs. **b,** Cyclability of the Li|TpPa-SO$_3$Li|Li, Li|p(BVIm-TFSI)/LiTFSI|Li, Li|TpPa-SO$_3$Li/p(BVIm-TFSI)|Li symmetric coin cells, tested under the current density of 0.3 mA cm$^{-2}$. **c**, Comparison of the PXRD patterns of TpPa-SO$_3$Li and DMTHA-Si-Li before and after the 600 cycle tests. **d**, Cyclability of the Li|DMTHA-Si-Li|Li and Li|DMTHA-Si-Li/p(BVIm-TFSI)|Li symmetric coin cells, tested under the current density

of 0.3 mA $cm^{-2}$. **e–h**, SEM images of Li anode surfaces of symmetric cells using SSEs of TpPa-$SO_3$Li/p(BVIm-TFSI) (underwent 600 cycles), DMTHA-Si-Li/p(BVIm-TFSI) (underwent 600 cycles), TpPa-$SO_3$Li (underwent 88 cycles), and DMTHA-Si-Li (underwent 125 cycles), respectively. The scale bar for all four images is placed in the upper right corner of (h). **i**, Rate performance of the Li|TpPa-$SO_3$Li/p(BVIm-TFSI)|LFP and Li|DMTHA-Si-Li/p(BVIm-TFSI)|LFP cells. **j, k**, Charge–discharge profiles of the Li|TpPa-$SO_3$Li/p(BVIm-TFSI)|LFP and Li|DMTHA-Si-Li/p(BVIm-TFSI)|LFP cells at different C rates, respectively. **l**, Cycling performance of the Li|TpPa-$SO_3$Li/p(BVIm-TFSI)|LFP and Li|DMTHA-Si-Li/p(BVIm-TFSI)|LFP cells at 1 C. **m, n,** Charge–discharge profiles of the Li|TpPa-$SO_3$Li/p(BVIm-TFSI)|LFP and Li|DMTHA-Si-Li/p(BVIm-TFSI)|LFP cells up to 800 cycles operated at 1 C, respectively.

We conducted a stability assessment of the iCOFs by removing the other components of the composites through washing and drying after the cycling test. A comparison of the PXRD patterns of TpPa-$SO_3$Li and DMTHA-Si-Li before and after the 600 cycle tests indicates that the iCOFs maintain their high crystallinity (**Fig. 5c**). The retention of high crystallinity in the PXRD patterns suggests that the structural integrity and ordered arrangement of the iCOFs fillers remain intact, after undergoing hundreds of cycles. Furthermore, we examined the surface of the Li metal anode subjected to charge–discharge cycles (**Fig. 5e–h**). The SEM images showed Li dendrite-free morphologies for the Li|TpPa-$SO_3$Li/p(BVIm-TFSI)|Li and Li|DMTHA-Si-Li/p(BVIm-TFSI)|Li symmetric coin cells, indicating that both of the TpPa-$SO_3$Li/p(BVIm-TFSI) and DMTHA-Si-Li/p(BVIm-TFSI) exhibited excellent suppression of Li dendrite formation. In contrast, pure iCOFs SSEs, both TpPa-$SO_3$Li and DMTHA-Si-Li, could not suppress the growth of Li dendrites. The dendrites had probably grown to go through the voids of the pure iCOFs SSEs.[48] This should be why the symmetric cells from pure iCOFs failed after around 100 cycles. The ASSLMB coin cells were assembled using either the TpPa-$SO_3$Li/p(BVIm-TFSI) or DMTHA-Si-Li/p(BVIm-TFSI) as SSEs in combination with $LiFePO_4$ (LFP) composite cathodes, denoted as Li|TpPa-$SO_3$Li/p(BVIm-TFSI)|LFP and Li|DMTHA-Si-

Li/p(BVIm-TFSI)|LFP. Note that we made composite cathodes by blending LFP and our SSEs to reduce the interfacial resistance between the cathode and composite SSEs (See Preparation of coin cells (CR 2032) in the **SI** for the detailed procedure) and applied them in all the cells in this study.[49] To further minimize the interfacial resistances between the composite cathode and composite SSEs, the assemblies were hot-pressed at a temperature of 60 ℃ and pressure of 20.6 MPa for an hour to be used in the battery cells.

Specific capacity and cyclic stability are the two most critical parameters for ASSLMBs evaluation. Thus, we first tested the rate performance of Li|TpPa-$SO_3$Li/p(BVIm-TFSI)|LFP and Li|DMTHA-Si-Li/p(BVIm-TFSI)|LFP at different C rates for every five cycles within a voltage range of 2.5–4.0 V (1 C = 170 mAh $g^{-1}$). The Li|TpPa-$SO_3$Li/p(BVIm-TFSI)|LFP delivered discharge capacities of 157.9, 149.6, 138.4, 126.6, and 86.4 mAh $g^{-1}$ at the rates of 0.2, 0.5, 1, 2 and 5 C, respectively (**Fig. 5i**). Similarly, the Li|DMTHA-Si-Li/p(BVIm-TFSI)|LFP exhibited discharge capacities of 159.8, 152.3, 140.8, 130.4 and 91.2 mAh $g^{-1}$ at the rates of 0.2, 0.5, 1, 2 and 5 C, respectively. The charge-discharge profiles of the Li|TpPa-$SO_3$Li/p(BVIm-TFSI)|LFP and Li|DMTHA-Si-Li/p(BVIm-TFSI)|LFP at different C rates were demonstrated in **Fig. 5j** and **5k**, respectively. The cyclic stability of the Li|TpPa-$SO_3$Li/p(BVIm-TFSI)|LFP and Li|DMTHA-Si-Li/p(BVIm-TFSI)|LFP were evaluated at a rate of 1 C at r.t. for 800 cycles. Li|TpPa-$SO_3$Li/p(BVIm-TFSI)|LFP and Li|DMTHA-Si-Li/p(BVIm-TFSI)|LFP cells demonstrated initial discharge specific capacities of 138.5 and 141.5 mAh $g^{-1}$. After 800 cycles, those respective cells showed capacity retentions of 81 and 87%, and Coulombic efficiencies remained as 99.7% and 98.9% (**Fig. 5l**). The charge-discharge profiles of Li|TpPa-$SO_3$Li/p(BVIm-TFSI)|LFP and Li|DMTHA-Si-Li/p(BVIm-

TFSI)|LFP cells up to 800 cycles are presented in **Fig. 5m** and **5n**. Such high capacities and capacity retention, > 80% up to 800 cycles, are highly desirable for the practical utilization of ASSLMBs operating at 1 C and r.t. Although several ASSLMBs employing COF-based SSEs have been reported, our cells from iCOFs/PIL composite stand out (**Table S4**). For the first time, we demonstrated stable operation, > 80% retention, at a higher rate, 1 C, for longer cycles, 800.

## Conclusion

We present a strategy for fabricating solvent- and plasticizer-free SSEs with exceptional ionic conductivity exceeding $10^{-3}$ S $cm^{-1}$ at r.t. with high $t_{Li^+} > 0.80$ using composites comprising anionic COFs, TpPa-$SO_3$Li or DMTHA-Si-Li, and cationic PIL, p(BVIm-TFSI). We found that the co-coordination and competitive coordination structures between $Li^+$, $TFSI^-$, anionic part of iCOFs, and polycation promoted rapid transport of $Li^+$ while rejecting $TFSI^-$ as confirmed by $^7$Li solid-state MAS NMR analyses and MD simulation studies. Also, the composite SSE method and the co-coordination mechanism are generalizable as can be seen from the cases of sulfonate COFs and silicate COFs. Both the TpPa-$SO_3$Li/p(BVIm-TFSI) and DMTHA-Si-Li/p(BVIm-TFSI) composite SSEs demonstrated remarkable suppression of Li dendrite formation, leading to stable plating and stripping up to 1,200 hours. Remarkably, the Li|DMTHA-Si-Li/p(BVIm-TFSI)|LFP coin cell exhibited an initial discharge capacity of 141.5 mAh $g^{-1}$ at r.t. and 1 C, along with an impressive capacity retention of 87% after 800 cycles. The high-performance composite SSEs hold great potential for practical applications in high-energy-density and high-safety ASSLMBs. In the future, the iCOF/PIL concept will be further

expanded to include iCOFs with advanced designs and PILs with different polymer structures and charges.

**Acknowledgment**

This work was supported by the Research Grants Council of the Hong Kong SAR Government (Early Career Scheme, #26309420 and General Research Fund, #16306921 and #16306022); the Department of Chemical and Biomolecular Engineering, HKUST (startup funding); and the 30 for 30 Research Initiative Scheme, VPRDO, HKUST.

**Conflict of interest**

The authors declare no conflict of interest.

**References**

(1) Wu, F.; Maier, J.; Yu, Y. Guidelines and trends for next-generation rechargeable lithium and lithium-ion batteries. *Chem. Soc. Rev.* **2020**, *49* (5), 1569–1614.
(2) Randau, S.; Weber, D. A.; Kötz, O.; Koerver, R.; Braun, P.; Weber, A.; Ivers-Tiffée, E.; Adermann, T.; Kulisch, J.; Zeier, W. G.; Richter, F. H,; Janek, J. Benchmarking the performance of all-solid-state lithium batteries. *Nat. Energy* **2020**, *5* (3), 259–270.
(3) Janek, J.; Zeier, W. G. Challenges in speeding up solid-state battery development. *Nat. Energy* **2023**, *8* (3), 230–240.
(4) Kim, K. J.; Balaish, M.; Wadaguchi, M.; Kong, L.; Rupp, J. L. M. Solid-State Li–Metal Batteries: Challenges and Horizons of Oxide and Sulfide Solid Electrolytes and Their Interfaces. *Adv. Energy Mater.* **2020**, *11* (1), 2002689.
(5) Ding, P.; Lin, Z.; Guo, X.; Wu, L.; Wang, Y.; Guo, H.; Li, L.; Yu, H. Polymer electrolytes and interfaces in solid-state lithium metal batteries. *Mater. Today* **2021**, *51*, 449–474.
(6) Wang, C.; Fu, K.; Kammampata, S. P.; McOwen, D. W.; Samson, A. J.; Zhang, L.; Hitz, G. T.; Nolan, A. M.; Wachsman, E. D.; Thangadurai. V.; Hu, L.; Garnet-Type Solid-State Electrolytes: Materials, Interfaces, and Batteries. *Chem. Rev.* **2020**, *120* (10), 4257–4300.
(7) Fan, L.-Z.; He, H.; Nan, C.-W. Tailoring inorganic–polymer composites for the mass production of solid-state batteries. *Nat. Rev. Mater.* **2021**, *6* (11), 1003–1019.

(8) Song, Z.; Chen, F.; Martinez-Ibañez, M.; Feng, W.; Forsyth, M.; Zhou, Z.; Armand, M.; Zhang, H. A reflection on polymer electrolytes for solid-state lithium metal batteries. *Nat. Commun.* **2023**, *14* (1), 4884.
(9) Luo, D.; Li, M.; Ma, Q.; Wen, G.; Dou, H.; Ren, B.; Liu, Y.; Wang, X.; Shui, L.; Chen, Z. Porous organic polymers for Li-chemistry-based batteries: functionalities and characterization studies. *Chem. Soc. Rev.* **2022**, 51(8), 2917–2938.
(10) Zhao, R.; Wu, Y.; Liang, Z.; Gao, L.; Xia, W.; Zhao, Y.; Zou, R. Metal–organic frameworks for solid-state electrolytes. *Energy. Environ. Sci.* **2020**, *13* (8), 2386–2403.
(11) Cao, Y.; Wang, M.; Wang, H.; Han, C.; Pan, F.; Sun, J. Covalent Organic Framework for Rechargeable Batteries: Mechanisms and Properties of Ionic Conduction. *Adv. Energy Mater.* **2022**, *12* (20), 2200057.
(12) Chen, L.; Ding, K.; Li, K.; Li, Z.; Zhang, X.; Zheng, Q.; Cai, Y.-P.; Lan, Y.-Q. Crystalline Porous Materials-based Solid-State Electrolytes for Lithium Metal Batteries. *EnergyChem* **2022**, *4* (3), 100073.
(13) Cote, A. P.; Benin, A. I.; Ockwig, N. W.; O'Keeffe, M.; Matzger, A. J.; Yaghi, O. M. Porous, crystalline, covalent organic frameworks. *Science* **2005**, *310* (5751), 1166–1170.
(14) Du, Y.; Yang, H.; Whiteley, J. M.; Wan, S.; Jin, Y.; Lee, S. H.; Zhang, W. Ionic Covalent Organic Frameworks with Spiroborate Linkage. *Angew. Chem., Int. Ed.* **2016**, *55* (5), 1737–1741.
(15) Sun, T.; Xie, J.; Guo, W.; Li, D. S.; Zhang, Q. Covalent–organic frameworks: advanced organic electrode materials for rechargeable batteries. *Adv. Energy Mater.* **2020**, *10* (19), 1904199.
(16) Liang, X.; Tian, Y.; Yuan, Y.; Kim, Y. Ionic Covalent Organic Frameworks for Energy Devices. *Adv. Mater.* **2021**, *33* (52), 2105647.
(17) Yu, F.; Ciou, J. H.; Chen, S.; Poh, W. C.; Chen, J.; Chen, J.; Haruethai, K.; Lv, J.; Gao, D.; Lee, P. S. Ionic covalent organic framework based electrolyte for fast-response ultra-low voltage electrochemical actuators. *Nat. Commun.* **2022**, *13* (1), 390.
(18) Tao, S.; Xu, H.; Xu, Q.; Hijikata, Y.; Jiang, Q.; Irle, S.; Jiang, D. Hydroxide Anion Transport in Covalent Organic Frameworks. *J. Am. Chem. Soc.* **2021**, *143* (24), 8970–8975.
(19) Zhao, J.; Ying, Y.; Wang, G.; Hu, K.; Di Yuan, Y.; Ye, H.; Liu, Z.; Lee, J. Y.; Zhao, D. Covalent organic framework film protected zinc anode for highly stable rechargeable aqueous zinc-ion batteries. *Energy Storage Mater.* **2022**, *48*, 82–89.
(20) Cao, Y.; Wu, H.; Li, G.; Liu, C.; Cao, L.; Zhang, Y.; Bao, W.; Wang, H.; Yao, Y.; Liu, S.; Pan, F.; Jiang, Z.; Sun, J. Ion Selective Covalent Organic Framework Enabling Enhanced Electrochemical Performance of Lithium-Sulfur Batteries. *Nano Lett.* **2021**, *21* (7), 2997–3006.
(21) Li, C.; Wang, D.-D.; Poon Ho, G. S. H.; Zhang, Z.; Huang, J.; Bang, K.-T.; Lau, C. Y.; Leu, S.-Y.; Wang, Y.; Kim, Y. Anthraquinone-Based Silicate Covalent Organic Frameworks as Solid Electrolyte Interphase for High-Performance Lithium–Metal Batteries. *J. Am. Chem. Soc.* **2023**, *145* (45), 24603–24614.
(22) Jeong, K.; Park, S.; Jung, G. Y.; Kim, S. H.; Lee, Y. H.; Kwak, S. K.; Lee, S. Y. Solvent-Free, Single Lithium-Ion Conducting Covalent Organic Frameworks. *J. Am. Chem. Soc.* **2019**, *141* (14), 5880–5885.
(23) Li, X.; Hou, Q.; Huang, W.; Xu, H.-S.; Wang, X.; Yu, W.; Li, R.; Zhang, K.; Wang, L.; Chen, Z. Solution-processable covalent organic framework electrolytes for all-solid-state Li–

organic batteries. *ACS Energy Lett.* **2020**, *5* (11), 3498–3506.
(24) Meng, F.; Bi, S.; Sun, Z.; Jiang, B.; Wu, D.; Chen, J. S.; Zhang, F. Synthesis of Ionic Vinylene-Linked Covalent Organic Frameworks through Quaternization-Activated Knoevenagel Condensation. *Angew. Chem., Int. Ed.* **2021**, *60* (24), 13614–13620.
(25) Li, X.; Tian, Y.; Shen, L.; Qu, Z.; Ma, T.; Sun, F.; Liu, X.; Zhang, C.; Shen, J.; Li, X.; Gao, L.; Xiao, S.; Liu, T.; Liu, Y.; Lu, Y. Electrolyte Interphase Built from Anionic Covalent Organic Frameworks for Lithium Dendrite Suppression. *Adv. Funct. Mater.* **2021**, *31* (22), 2009718.
(26) Hu, Y.; Dunlap, N.; Wan, S.; Lu, S.; Huang, S.; Sellinger, I.; Ortiz, M.; Jin, Y.; Lee, S. H.; Zhang, W. Crystalline Lithium Imidazolate Covalent Organic Frameworks with High Li-Ion Conductivity. *J. Am. Chem. Soc.* **2019**, *141* (18), 7518–7525.
(27) Zhang, S. Y.; Zhuang, Q.; Zhang, M.; Wang, H.; Gao, Z.; Sun, J. K.; Yuan, J. Poly(ionic liquid) composites. *Chem. Soc. Rev.* **2020**, *49* (6), 1726–1755.
(28) Chen, F.; Wang, X.; Armand, M.; Forsyth, M. Cationic polymer-in-salt electrolytes for fast metal ion conduction and solid-state battery applications. *Nat. Mater.* **2022**, *21* (10), 1175–1182.
(29) Wang, X.; Chen, F.; Girard, G. M. A.; Zhu, H.; MacFarlane, D. R.; Mecerreyes, D.; Armand, M.; Howlett, P. C.; Forsyth, M. Poly(Ionic Liquid)s-in-Salt Electrolytes with Co-coordination-Assisted Lithium-Ion Transport for Safe Batteries. *Joule* **2019**, *3* (11), 2687–2702.
(30) Ma, F.; Zhang, Z.; Yan, W.; Ma, X.; Sun, D.; Jin, Y.; Chen, X.; He, K. Solid polymer electrolyte based on polymerized ionic liquid for high performance all-solid-state lithium-ion batteries. *ACS Sustainable Chem. Eng.* **2019**, *7* (5), 4675–4683.
(31) Qian, W.; Texter, J.; Yan, F. Frontiers in poly (ionic liquid) s: syntheses and applications. *Chem. Soc. Rev.* **2017**, *46* (4), 1124–1159.
(32) Kandambeth, S.; Mallick, A.; Lukose, B.; Mane, M. V.; Heine, T.; Banerjee, R. Construction of Crystalline 2D Covalent Organic Frameworks with Remarkable Chemical (Acid/Base) Stability via a Combined Reversible and Irreversible Route. *J. Am. Chem. Soc.* **2012**, *134* (48), 19524–19527.
(33) Roeser, J.; Prill, D.; Bojdys, M. J.; Fayon, P.; Trewin, A.; Fitch, A. N.; Schmidt, M. U.; Thomas, A. Anionic silicate organic frameworks constructed from hexacoordinate silicon centres. *Nat. Chem.* **2017**, *9* (10), 977–982.
(34) Chen, N.; Hu, C.; Wang, H. H.; Kim, S. P.; Kim, H. M.; Lee, W. H.; Bae, J. Y.; Park, J. H.; Lee, Y. M. Poly(Alkyl-Terphenyl Piperidinium) Ionomers and Membranes with an Outstanding Alkaline-Membrane Fuel-Cell Performance of 2.58 W $cm^{-2}$. *Angew. Chem., Int. Ed.* **2021**, *60* (14), 7710–7718.
(35) Wei, P.-F.; Qi, M.-Z.; Wang, Z.-P.; Ding, S.-Y.; Yu, W.; Liu, Q.; Wang, L.-K.; Wang, H.-Z.; An, W.-K.; Wang, W. Benzoxazole-Linked Ultrastable Covalent Organic Frameworks for Photocatalysis. *J. Am. Chem. Soc.* **2018**, *140* (13), 4623–4631.
(36) Guo, D.; Shinde, D. B.; Shin, W.; Abou-Hamad, E.; Emwas, A. H.; Lai, Z.; Manthiram, A. Foldable Solid-State Batteries Enabled by Electrolyte Mediation in Covalent Organic Frameworks. *Adv. Mater.* **2022**, 2201410.
(37) Yao, Y.; Cao, Y.; Li, G.; Liu, C.; Jiang, Z.; Pan, F.; Sun, J. Enhanced Electrochemical Performance of Poly(ethylene oxide) Composite Polymer Electrolyte via Incorporating Lithiated Covalent Organic Framework. *Transactions of Tianjin University* **2021**, *28* (1), 67–72.
(38) Chen, H.; Tu, H.; Hu, C.; Liu, Y.; Dong, D.; Sun, Y.; Dai, Y.; Wang, S.; Qian, H.; Lin, Z.

Cationic covalent organic framework nanosheets for fast Li-ion conduction. *J. Am. Chem. Soc.* **2018**, *140* (3), 896–899.
(39) Dong, D.; Zhang, H.; Zhou, B.; Sun, Y.; Zhang, H.; Cao, M.; Li, J.; Zhou, H.; Qian, H.; Lin, Z. Porous covalent organic frameworks for high transference number polymer-based electrolytes. *Chem. Commun.* **2019**, *55* (10), 1458–1461.
(40) Guo, Z.; Zhang, Y.; Dong, Y.; Li, J.; Li, S.; Shao, P.; Feng, X.; Wang, B. Fast ion transport pathway provided by polyethylene glycol confined in covalent organic frameworks. *J. Am. Chem. Soc.* **2019**, *141* (5), 1923–1927.
(41) Li, Z.; Liu, Z.-W.; Mu, Z.-J.; Cao, C.; Li, Z.; Wang, T.-X.; Li, Y.; Ding, X.; Han, B.-H.; Feng, W. Cationic covalent organic framework based all-solid-state electrolytes. *Mater. Chem. Front.* **2020**, *4* (4), 1164–1173.
(42) Li, Z.; Liu, Z. W.; Li, Z.; Wang, T. X.; Zhao, F.; Ding, X.; Feng, W.; Han, B. H. Defective 2D covalent organic frameworks for postfunctionalization. *Adv. Funct. Mater.* **2020**, *30* (10), 1909267.
(43) Kang, T. W.; Lee, J.-H.; Lee, J.; Park, J. H.; Shin, J.-H.; Ju, J.-M.; Lee, H.; Lee, S. U.; Kim, J.-H. An Ion-Channel-Restructured Zwitterionic Covalent Organic Framework Solid Electrolyte for All-Solid-State Lithium-Metal Batteries. *Adv. Mater.* **2023**, *35* (30), 2301308.
(44) Gong, W.; Ouyang, Y.; Guo, S.; Xiao, Y.; Zeng, Q.; Li, D.; Xie, Y.; Zhang, Q.; Huang, S. Covalent Organic Framework with Multi-Cationic Molecular Chains for Gate Mechanism Controlled Superionic Conduction in All-Solid-State Batteries. *Angew. Chem., Int. Ed.* **2023**, *62* (25), e202302505.
(45) Angell, C.; Liu, C.; Sanchez, E. Rubbery solid electrolytes with dominant cationic transport and high ambient conductivity. *Nature* **1993**, *362* (6416), 137–139.
(46) Xu, W.; Wang, L.; Angell, C. “PolyMOB”-lithium salt complexes: From salt-in-polymer to polymer-in-salt electrolytes. *Electrochim. Acta* **2003**, *48*, 2037–2045.
(47) Dong, P.; Zhang, X.; Hiscox, W.; Liu, J.; Zamora, J.; Li, X.; Su, M.; Zhang, Q.; Guo, X.; McCloy, J.; Song, M.-K. Toward High-Performance Metal–Organic-Framework-Based Quasi-Solid-State Electrolytes: Tunable Structures and Electrochemical Properties. *Adv. Mater.* **2023**, *35* (32), 2211841.
(48) Cao, D.; Sun, X.; Li, Q.; Natan, A.; Xiang, P.; Zhu, H. Lithium dendrite in all-solid-state batteries: growth mechanisms, suppression strategies, and characterizations. *Matter* **2020**, *3* (1), 57–94.
(49) Al-Salih, H.; Houache, M. S. E.; Baranova, E. A.; Abu-Lebdeh, Y. Composite Cathodes for Solid-State Lithium Batteries: “Catholytes” the Underrated Giants. *Adv. Energy Sustainability Res.* **2022**, *3* (8), 2200032.